

www.acsnano.org

Anodized Nickel Foam for Oxygen Evolution Reaction in Fe-Free and Unpurified Alkaline Electrolytes at High Current Densities

Yoon Jun Son, Kenta Kawashima, Bryan R. Wygant, Chon Hei Lam, James N. Burrow, Hugo Celio, Andrei Dolocan, John G. Ekerdt, and C. Buddie Mullins*



Cite This: ACS Nano 2021, 15, 3468–3480



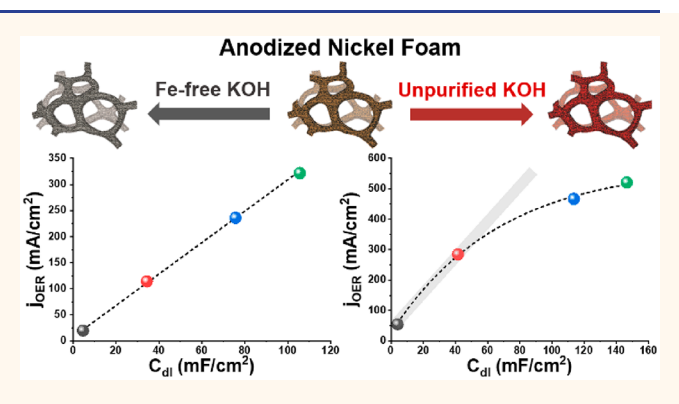
ACCESS

Metrics & More

Article Recommendations

si Supporting Information

ABSTRACT: To achieve practically high electrocatalytic performance for the oxygen evolution reaction (OER), the active surface area should be maximized without severely compromising electron and mass transport throughout the catalyst electrode. Though the importance of electron and mass transport has been studied using low surface area catalysts under low current densities (~tens of mA/cm²), the transport properties of large surface area catalysts under high operating current densities (~500 mA/cm²) for practical OER catalysis have rarely been explored. Herein, three-dimensional (3D) hierarchically porous anodized nickel foams (ANFs) with large and variable surface areas were synthesized *via* electrochemical anodization of 3D nickel foam and applied as OER electro-



catalysts in Fe-free and unpurified KOH electrolytes. Using Fe-free and in situ Fe-doped ANF that were prepared in Fe-free and unpurified electrolytes, respectively, we investigated the interdependent effects of active surface area and transport properties on OER activity under practically high current densities. While activity increased linearly with active surface area for Fe-free ANF, the activity of Fe-doped ANF showed a nonlinear increase with active surface area due to lower electrocatalytic activity enhancement. Detailed investigations on the possible factors (Fe incorporation, mass transport, and electron transport) identified that electron transport limitations played the major role in restricting the activity enhancement with increasing active surface area for Fe-doped ANF, although Fe-doped ANF has electron transport properties better than those of Fe-free ANF. This study exemplifies the growing significance of electron transport properties in large surface area catalysts, especially those with superb intrinsic catalytic activity and high operating current density.

KEYWORDS: oxygen evolution reaction, electrocatalyst, water splitting, anodized nickel foam, electron and mass transport, Fe-free electrolyte, unpurified electrolyte

lectrochemical water splitting, consisting of the cathodic hydrogen evolution reaction (HER) and anodic oxygen evolution reaction (OER), is a promising energy technology for clean hydrogen production. Whereas the HER involves the transfer of only two electrons, the four-electron transfer mechanism of the OER is more complicated and kinetically sluggish. Thus, the development of highly active OER electrocatalysts is essential for efficient electrochemical water splitting. Although noble-metal-based oxides (e.g., IrO₂ and RuO₂) show high OER activity in acidic environments, the high cost and scarcity of these catalysts hinder their large-scale applications. The high regard, great attention has been directed to the OER in alkaline media where nonprecious transition metal (e.g., Ni, Co, and Fe)-based electrocatalysts remain highly active and stable. As a supplementation of the catalysts remain highly active and stable.

Several types of alkaline OER catalysts have been studied, such as monometallic or bimetallic oxides and (oxy)-hydroxides, ^{6,7} transition metal compounds (*e.g.*, carbides, pnictides, and chalcogenides), ^{8,9} *etc.* Among these, NiFebased catalysts have shown the best OER activity in alkaline media. ^{10–13} It has been reported that the presence of both Fe and Ni is the key to superb OER activity of NiFe-based OER

Received: December 23, 2020 Accepted: January 22, 2021 Published: January 29, 2021





catalysts and that Fe sites in Ni_{1-x}Fe_xOOH act as active sites for the OER. 14-16 The optimal composition of NiFe-based catalysts varies depending on the synthetic method but lies generally in the range of 10–25% Fe. 14,17 Corrigan found that unintentionally introduced Fe impurities in KOH electrolyte (ppm scale) would significantly enhance the OER activity of NiOOH. 18 Trotochaud et al. also confirmed that Fe impurities in many commercial KOH electrolytes are incorporated into Ni(OH)₂ spontaneously during cyclic voltammetry (CV) cycling and showed the formation of NiFeOOH throughout the electrolyte-permeable structure of Ni(OH)₂. ¹⁹ Friebel et al. found that Fe can be absorbed through the Ni(OH)2 film up to a solubility limit of ~25% Fe. 14 All of these previous studies indicate that NiFe-based catalysts with satisfactory Fe composition can be easily prepared by in situ Fe incorporation during OER cycling of Ni-based materials in unpurified KOH electrolytes.

To achieve high OER current densities for industrial applications with minimized overpotential, increasing the number of active sites *via* high catalyst loadings is unavoidable even for electrocatalysts with high intrinsic catalytic activity. However, when increasing catalyst loadings, activity enhancement is hindered by both mass (reactant and product) and electron transport limitations and by low active site utilization upon increasing the catalyst layer thickness. This leads to an initial nonlinear increase in activity with increased loading, which eventually plateau's or even decreases at a critical value of loading due to these transport constraints. ^{20,21}

In this regard, several recent studies have examined the influence of electron and mass transport limitations for the HER and OER and suggested strategies for addressing the transport limitations through the addition of conductive carbonaceous supports or the engineering of the catalyst electrode morphology at the micro/nanometer scale. Chung et al. used molybdenum sulfide with carbon additives to examine the influence of electrical conductivity on the HER activity of the catalyst.²² Bediako et al. investigated the effect of protoncoupled electron transport on the OER activity using cobaltbased oxide catalysts.²³ Batchellor et al. showed the importance of good connectivity in micro/nanostructured Ni-Fe (oxy)hydroxide catalyst films for improving electrical conductivity.² Morales-Guio et al. studied the resistance of electron and ion transport as a function of loading of CoFeO_r catalyst for the OER.²¹ However, all of these insightful studies of transport properties were conducted using relatively low surface area catalyst films on two-dimensional (2D) substrates that operate at low current densities (~tens of mA/cm²). Given that large surface area catalyst electrodes that can deliver high current densities (>500 mA/cm²) are employed for the practical OER catalysis required for commercial electrolyzers, 25-27 it is imperative to investigate the influence of transport limitations on OER activity using large surface area catalysts and practically high operating current densities, as well as to determine an effective strategy for addressing the transport

Herein, we present the morphological engineering of threedimensional (3D) nickel foam (NF) *via* electrochemical anodization as a strategy for increasing the number of active sites while minimizing detrimental electron and mass transport limitations. The anodized NF (ANF) had a hierarchically porous structure consisting of micrometer- and nanometersized pores and was directly applied as an OER electrocatalyst in Fe-free and unpurified (Fe-containing) 1 M KOH electrolytes. Using the prepared ANF catalysts, we conducted a systematic analysis to reveal how morphological engineering and the resulting transport properties affect the OER activity. Our study based on ANF in two different electrolytes has advantages for understanding the effects of transport properties for practical OER catalysts for the following reasons. First, ANF can achieve a large surface area with a relatively small thickness compared to a 2D film due to its 3D hierarchically porous structure. Also, the surface area of ANF can be easily controlled by changing anodization time while maintaining the morphology. These characteristics of ANF deconvolute the complex relations of active surface area and transport properties, thereby enabling us to observe the effects of transport properties on OER activity as a function of surface area under high current densities, while minimizing other complicating factors, such as severe oxygen bubble issues^{28–31} and low utilization of catalytic active sites by high catalyst loadings (also known as overgrowth).20 Second, previous studies of transport limitations have been carried out using the same composition of the catalyst with different loadings. 22,24,32 However, in our study, using the same ANF samples, two different compositions of catalysts, Fe-free and Fe-doped ANFs, were prepared in situ in Fe-free and unpurified 1 M KOH electrolytes, respectively, via OER precycling. Using these catalysts, we elucidated the actual contribution of the transport properties to the OER activity for two different compositions of catalysts that have different intrinsic catalytic activity and electron transport properties.

RESULTS AND DISCUSSION

Optimization of Anodization Condition on 3D Nickel Foam. Electrochemical anodization is a very simple and attractive technique to form self-organized nanoporous oxide structures using various metal substrates including Al,³³ Ti,³⁴ and others. During anodization in an electrolyte solution containing ethylene glycol, water, and NH₄F, oxide formation (via oxidation of the target metal with water under positive bias) and dissolution of the formed metal oxide (via formation of MF_r complexes by the F ion of NH₄F), which is accelerated under an electric field (e-field), occur at the same time; balancing the rate of these two reactions is the key to successful nanostructuring. 35-37 In this work, we aimed to grow a thick and nanoporous structure of nickel oxide uniformly on the 3D NF substrate via anodization, thereby creating a 3D hierarchical porous structure consisting of micrometer-scale pores among the branches of 3D NF and nanometer-scale pores on each NF branch. However, unlike common metal substrates, there are additional challenges for the anodization of 3D NF. First, as Ni is active toward water oxidation, water oxidation occurs under positive bias during anodization, and the oxygen bubbles produced from Ni hinder the formation of an ordered porous structure on the Ni substrate.³⁶ Second, as opposed to the 2D flat substrates commonly employed for anodization (e.g., foil, film, etc.), 38 3D substrates can generate uneven e-fields during anodization due to the varying distance between the counter electrode and the surface of the 3D working electrode, potentially leading to nonhomogeneous anodization on the 3D substrate. As a result, it is critical to balance the rate of oxide formation and dissolution while minimizing the OER and e-field heterogeneity in order to grow nanostructures on 3D NF substrates uniformly. To do so, we controlled the water content and F concentration of the electrolyte, as well as the average strength

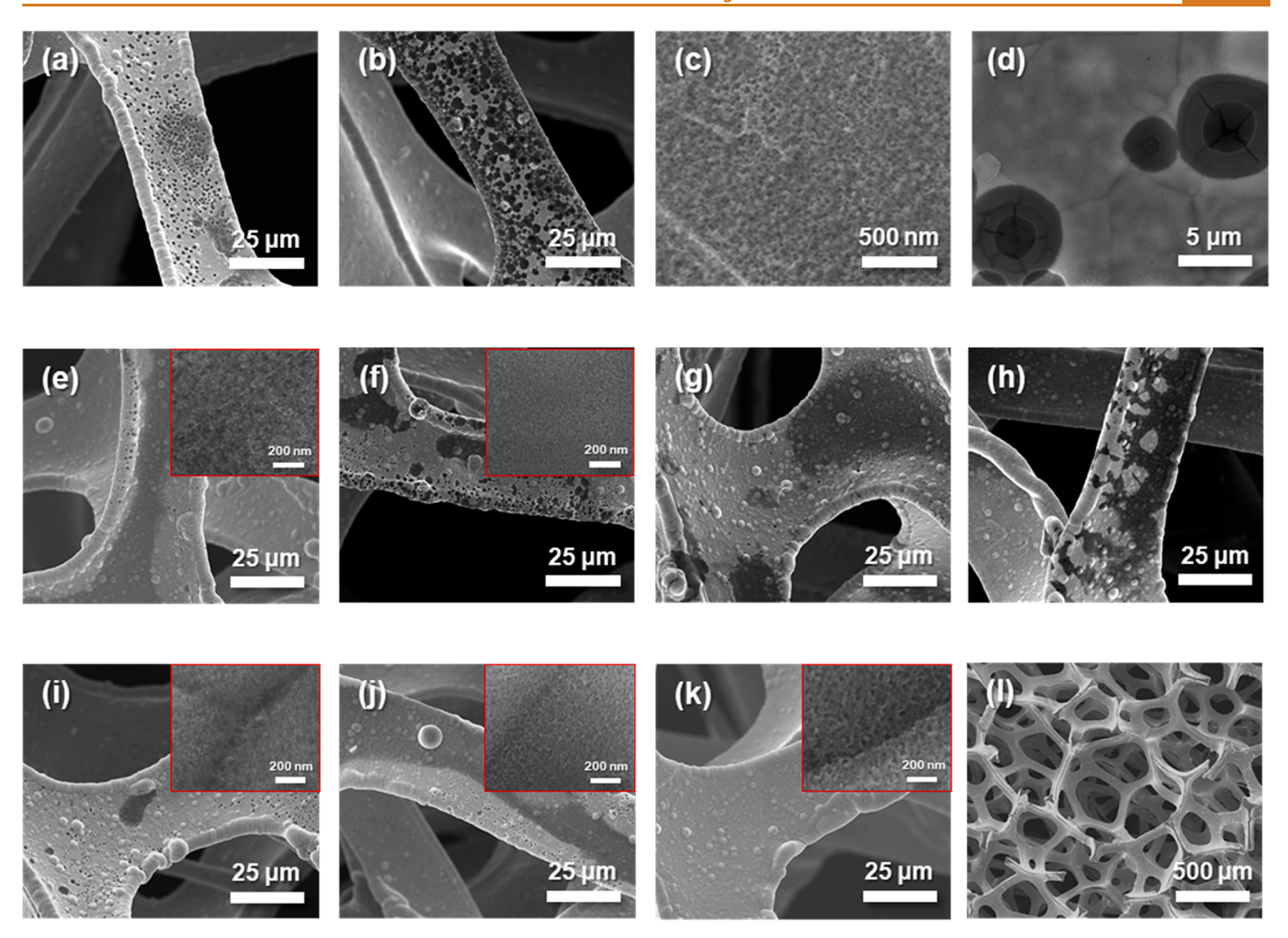


Figure 1. SEM images of ANF under different anodization conditions (NH₄F concentration/H₂O content/applied voltage/distance between electrodes/anodization time): (a–d) 75 mM/2 vol %/40 V/1.8 cm/x h: (a) 0.5 h, (b) 2 h, (c,d) 2h (the surface of NF branch at high magnification); (e,f) x mM/2 vol %/30 V/2.5 cm/0.5 h: (e) 25 mM, (f) 50 mM, (g) 75 mM, (h) 150 mM; (i–l) 50 mM/x vol %/20–30 V/2.5 cm/0.5 h: (i) 2 vol %/20 V, (j) 3 vol %/30 V, (k) 4 vol %/30 V, (l) 4 vol %/30 V (overview at low magnification).

of the applied e-field, which is proportional to the applied voltage and inversely proportional to the distance between the working and counter electrode.

Figure 1a-d shows the top-view scanning electron microscopy (SEM) images of ANF prepared using a previously reported anodization condition for a 2D nickel foil.³⁹ After anodization, the nanoporous structures with pores on the order of tens of nanometers were successfully formed on the NF branches (Figure 1c). However, we also observed that black spots were created along with the formation of nanoporous structures during anodization and that the proportion of black spots increased with increasing anodization time from 0.5 to 2 h (Figure 1a,b). From the magnified image of the black spots in Figure 1d, cracks were apparent on the black spots. This nonuniform generation of black spots can be related to a nonuniform e-field on the NF substrate during anodization, due to its nonflat 3D structure. By comparing ANF samples prepared by applying a lower e-field (Figure 1g) versus a higher e-field (Figure 1a,b), we found that lower e-fields created fewer black spots on the NF, implying less localization of the electric field for lower applied e-fields. To better understand the identity of the black spots, ANF samples that were synthesized using different concentrations of NH₄F in the electrolyte were also compared. Figure 1e-h shows that the surface density of black spots on the NF branches changed in proportion to

NH₄F concentration. Considering that a higher concentration of F can accelerate the rate of oxide dissolution, especially on the areas under a stronger e-field, where the mass transfer of the F⁻ ion is facilitated, ³⁶ this result implies that nonuniform generation of these black spots resulted from the fast kinetics of oxide dissolution at the points under stronger local e-fields. Though black spots have nearly the same chemical composition as nonblack spots according to energy-dispersive X-ray (EDX) spectroscopy point analyses (Figure S1), the nonuniform generation of black spots can be disadvantageous due to the following reasons: (1) poor anodization of the NF overall because of selective anodization on spots under a stronger e-field and thereby less anondization on spots under a weaker e-field, which can lead to the failure to grow a thick porous structure under a weaker e-field, and (2) accelerated oxide dissolution on higher e-field spots that can cause an imbalance between the rate of oxide formation and the rate of oxide dissolution, resulting in the collapse of the porous structure as shown in Figure 1d.

To form nanoporous structures uniformly on the 3D NF substrate, we used an electrolyte with 50 mM NH_4F for anodization. ANF made using 50 mM NH_4F not only had fewer black spots compared to ones using higher concentrations of NH_4F but also formed a clear nanoporous structure compared to ANF prepared using 25 mM NH_4F . To further

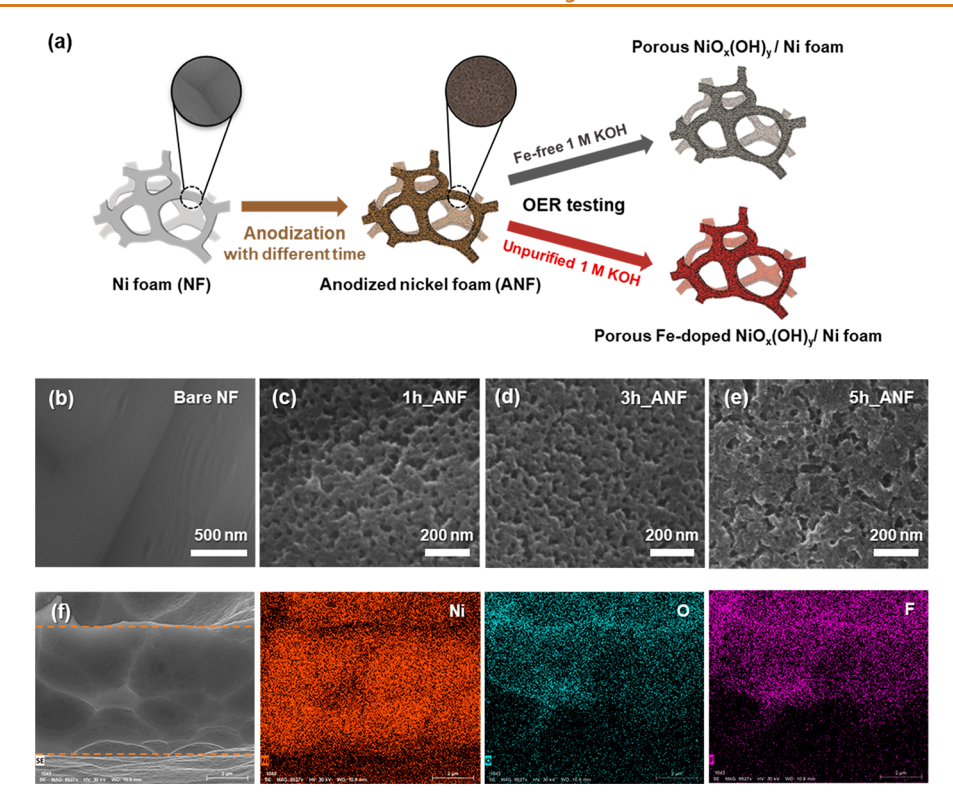


Figure 2. (a) Schematic illustration of preparation of ANF with different anodization time and its application to OER in Fe-free and unpurified 1 M KOH. (b-e) Top-view SEM images of bare NF and as-prepared 1h, 3h, and 5h_ANF. (f) Cross-sectional SEM and EDX mapping images of Ni, O, and F of as-prepared 5h_ANF after Ar-ion milling (orange dash lines indicate the NF branch).

suppress the formation of black spots for ANF using 50 mM $\mathrm{NH_4F}$, the e-field was reduced by decreasing the applied voltage from 30 to 20 V. As shown in Figure 1i, however, even though black spot formation could be reduced, the growth of a clear nanoporous structure was suppressed, probably due to the weak e-field. Thus, instead of lowering the e-field, the water content in the electrolyte was adjusted from 2 to 4 vol % to increase the oxide formation rate and thereby balance the oxide formation and dissolution rate (Figure 1j,k). Consequently, for ANF using 4 vol % of water content, the density of black spots could be reduced successfully while creating and maintaining a nanostructure well (Figure 1k,l). Thus, in the following experiments, we employed the optimized anodization condition (50 mM $\mathrm{NH_4F/4}$ vol % water/applied voltage: 30 V/distance between electrodes: 2.5 cm).

Characterization of Anodized Nickel Foam. Figure 2a presents the schematic illustration for the overall procedures of this study. First, hierarchical porous ANF samples with different anodization times (xh ANF, where xh indicates 1, 3, 5, and 7 h of anodization time) were prepared using the optimized anodization condition. Here, anodization time was controlled to change the thickness of the porous oxide layer and the resulting surface area of the electrode while maintaining the morphology. 36,39 Then, the prepared xh ANF samples were directly applied as OER electrocatalysts in two different electrolytes, Fe-free and unpurified (Fecontaining) 1 M KOH. Figure S2 presents digital photographs of as-prepared xh_ANF samples. Figure 2b-e shows top-view SEM images of bare NF and as-prepared xh_ANF samples. Whereas bare NF has a smooth surface, xh ANF samples have a nanoporous structure with a similar nanoporosity of 0.234 to 0.263 and a mean pore size of 21.4 to 29.4 nm (Figure S3). On the other hand, as shown in Figure S4, even though 7h ANF

has a rough surface compared to bare NF, it was difficult to observe the nanoporous structure on the surface.

The chemical composition and state of as-prepared xh ANF were analyzed by X-ray photoelectron spectroscopy (XPS) (Figure S5a-d). For bare NF, Ni 2p_{3/2} showed a metallic Ni peak at a binding energy (BE) of 852.8 eV,40 as well as multiplet-split peaks from the Ni oxide layer, which forms on the surface of bare NF under ambient conditions, at 853.9 eV from NiO and 855.8 eV from $NiO_x(OH)_{yy}$ whose BE is between those of $Ni(OH)_2$ and NiOOH.^{41–44} This matches with the O 1s signal of bare NF showing two peaks at BEs of 529.7 and 531.1 eV, which are indicative of the Ni-O bond of NiO and Ni(OH)₂ from defective nickel oxide with hydroxyl groups absorbed on the surface, respectively. 45 For all xh ANF samples, an F 1s signal was detected together with Ni and O due to the presence of NH₄F in the anodization electrolyte, and their Ni 2p, O 1s, and F 1s spectra had the same shape and BE, implying their identical chemical composition. The F 1s spectra displayed a peak at 684 eV, which belongs to the Ni-F bond. 46,47 Also, xh_ANF had a Ni 2p_{3/2} peak at 856.4 eV, which is between the 855.8 eV peak of $NiO_x(OH)_y$ and the ~857.6 eV peak of NiF_2 . This positive BE shift for Ni 2p_{3/2} from ANF of 0.6 eV compared to NiO_x(OH)_y can be explained by additional electron density donation from Ni to F, which has an electronegativity higher than that of O. The O 1s spectra for xh ANF showed a peak at 531.1 eV, which is assignable to $NiO_x(OH)_y$. Based on these XPS results, it was found that F-doped $NiO_x(OH)_y$ was synthesized by anodization of NF. Additionally, the absence of Fe impurities in asprepared xh ANF was confirmed from the Fe 3p region. X-ray diffraction (XRD) analysis was performed to characterize the crystal structure of the as-prepared xh ANF (Figure S6). However, like bare NF, all the xh ANF exhibited only metallic

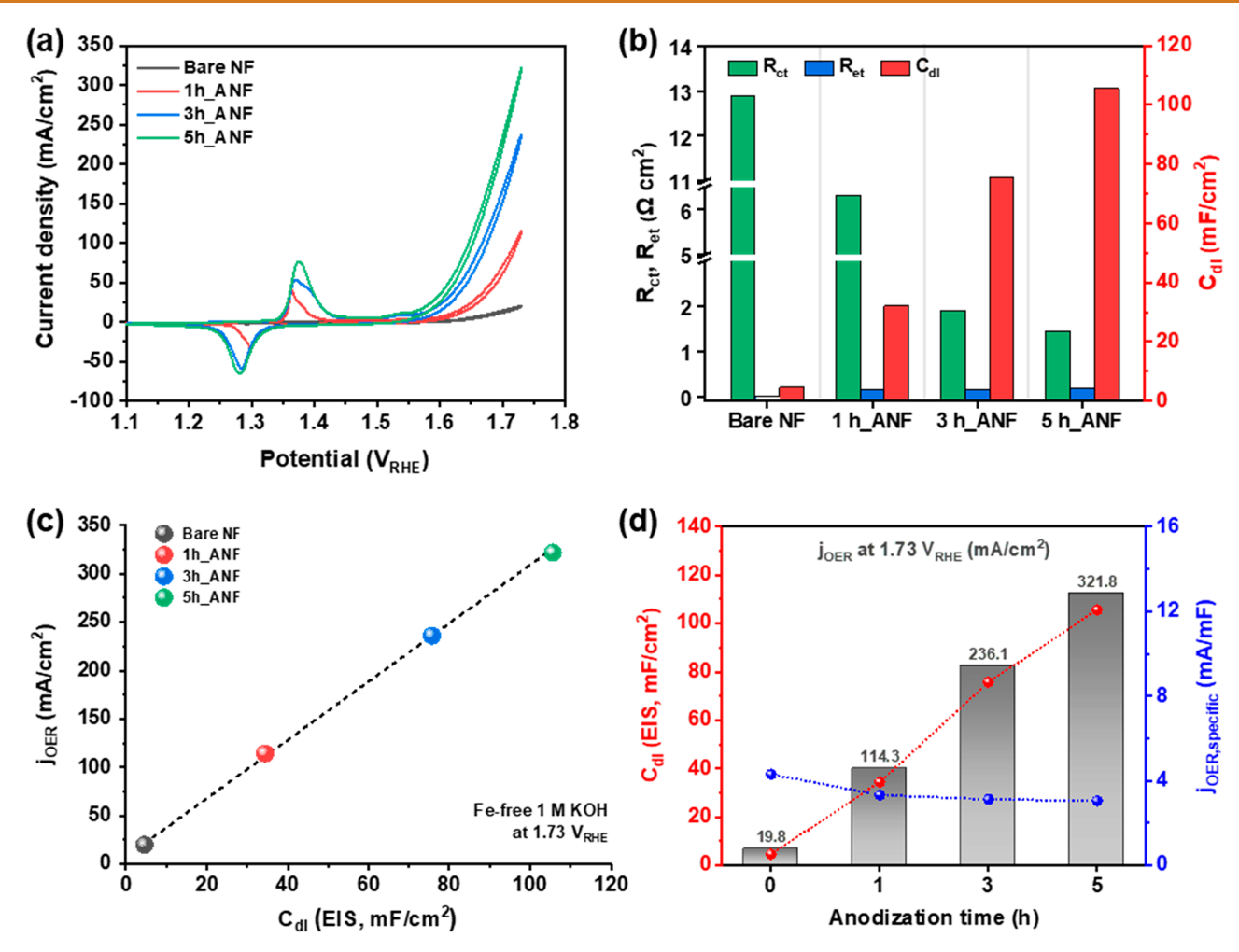


Figure 3. Electrochemical analyses of xh_ANF in Fe-free 1 M KOH electrolyte. (a) CV curves. (b) Electrochemical parameters obtained from EIS fitting at 1.63 V_{RHE} . (c) Plot of j_{OER} at 1.73 V_{RHE} with regard to C_{dl} . (d) Correlation between C_{dl} , j_{OER} , and $j_{OER,specific}$ and anodization time.

Ni peaks at 2θ degrees of 44.8 and 52.2. This signifies that porous F-doped NiO_x(OH)_y has an amorphous structure and that bulk Ni metal from the NF remains underneath the porous F-doped NiO_x(OH), layer. The transmission electron microscopy (TEM) images for the anodized layer scraped off from the as-prepared 3h ANF sample by ultrasonication in ethanol also revealed no lattice fringes, and its selected area electron diffraction (SAED) pattern displayed diffuse rings, which indicate its amorphous feature (Figure S7). Figure 2f displays the cross-sectional SEM image of the branch of 5h ANF, which was prepared by Ar-ion milling and its EDX mapping images. By comparing the Ni signal with the O and F signals, it was found that the porous F-doped $NiO_x(OH)_y$ layer was grown up to $\sim 3.2 \mu m$ out of the total thickness of the Ni branch of $\sim 6.2 \mu \text{m}$, indicating a F-doped NiO_x(OH)_v/Ni structure for the as-prepared ANF, which is consistent with the results from XPS and XRD. Furthermore, it was observed that the thickness of the porous F-doped NiO_x(OH), layer increased with anodization time (Figure S8).

Electrochemical Analyses in Fe-Free 1 M KOH Electrolyte. The electrochemical characteristics and OER activity of xh_ANF were first investigated by CV in Fe-free 1 M KOH aqueous electrolyte using a three-electrode system: xh_ANF as the working electrode, Hg/HgO as the reference electrode, and Pt foil as the counter electrode. Before the

measurement of OER activity, precycling using CV was performed for xh ANF in the potential range of 1.1 to 1.73 V versus the reversible hydrogen electrode (V_{RHE}) until its CV curve reached a steady state. Also, 85% iR correction was performed for all of the CV analyses. From the CV curves in Figure 3a, the oxidative redox peak occurring around 1.37 V_{RHE} is attributed to the transition of Ni(OH)₂ (Ni²⁺) to NiOOH (Ni³⁺), whereas a small oxidative peak at 1.53 V_{RHE} is assigned to the formation of Ni⁴⁺ oxidation state, which is a feature observed in Fe-free NiO_x(OH)_y (Figure S9). 19 Also, the OER activity and redox charge passed for the Ni²⁺ to Ni³⁺ transition of xh ANF increased gradually with anodization time, and $5h_ANF$ showed the highest OER current density (j_{OER}) of 321.8 mA/cm 2 at 1.73 V_{RHE} . However, further anodization after 5 h instead led to the decrease of j_{OER} and a redox charge for the Ni²⁺ to Ni³⁺ transition for 7h ANF (Figure S10a). Additionally, Figure S11 shows that CV results using a graphite counter electrode were consistent with those carried out with the Pt foil counter electrode, ensuring that there was no issue of using the Pt counter electrode for OER testing.

To investigate the factors underpinning the above OER activity trend, electrochemical impedance spectroscopy (EIS) analysis was conducted at 1.63 V_{RHE} . Figure S12a displays the Nyquist plots of the EIS spectra for xh_ANF consisting of two semicircles. The first semicircle at higher frequencies originates

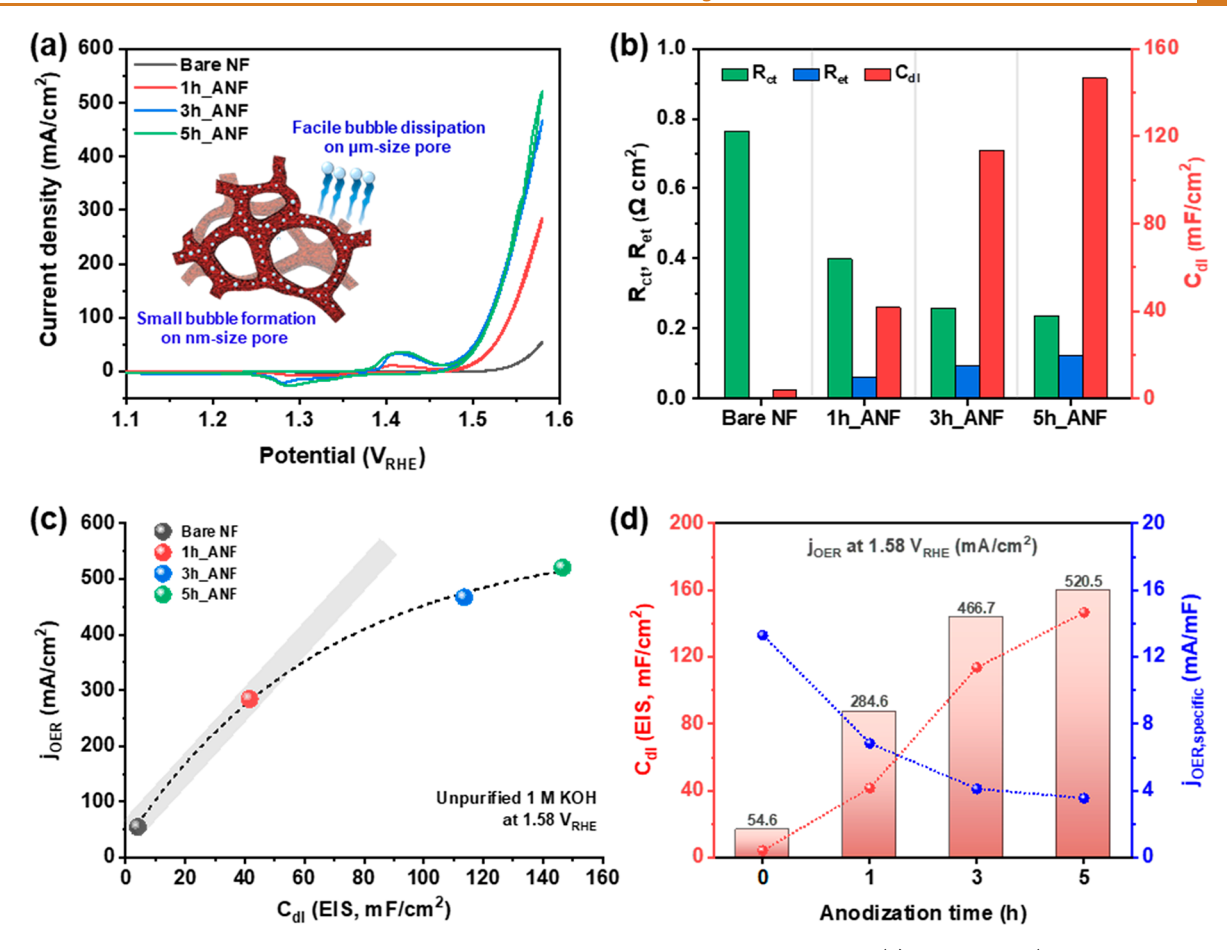


Figure 4. Electrochemical analyses of xh_ANF samples in unpurified 1 M KOH electrolyte. (a) CV curves (inset shows facile bubble dissipation of xh_ANF). (b) Electrochemical parameters obtained from EIS fitting at 1.58 V_{RHE} . (c) Plot of j_{OER} at 1.58 V_{RHE} with regard to C_{dl} . (d) Correlation between C_{dl} , j_{OER} , and $j_{OER,specific}$ and anodization time.

from the contact impedance between the xh ANF and the titanium clip and is about the same size for all of the xh ANF samples. 32,51 The second semicircle at lower frequencies is related to the activity of the electrocatalyst and is usually regarded as charge transfer resistance (R_{ct}) at the interface between the electrocatalyst and electrolyte. However, it is notable that the shape of the second semicircle of xh ANF gradually becomes asymmetrical in proportion to the anodization time, while that of bare NF has a perfectly symmetrical shape, as shown in Figure S12b-e. This asymmetrical feature is associated with the electron transport resistance ($R_{\rm ef}$) through the catalyst layer. ^{32,52,53} To decouple the effects of electron transport property (or R_{et}) and catalytic activity (or R_{ct}) in the second semicircle, the transmission line model in Figure S13a and the corresponding equivalent circuit in Figure S13b, which were previously applied to model the porous electrodes, were adapted for EIS fitting of 1h, 3h, and Sh_ANF (see Supporting Information for details related to EIS analysis). 21,32,51-55 For EIS fitting of bare NF, the simple equivalent circuit in Figure S13c was employed.

Figure 3b and Table S1 present the electrochemical parameters obtained from EIS fitting. The double layer capacitance ($C_{\rm dl}$) of xh_ANF calculated from EIS, which can be used to deduce the electrochemically active surface area of the electrocatalyst, increased with anodization time from 4.6 mF/cm² for bare NF to 105.6 mF/cm² for Sh_ANF. This can be explained by the increase of thickness of the porous oxide layer with increasing anodization time, implying successful

anodization. 36,39 Also, in Figure S14, the value of C_{dl} for xh ANF determined through CV in the nonfaradaic potential region also showed a similar increasing trend with anodization time, but was 3 orders of magnitude lower than those from EIS analysis and showed too small a difference in $C_{\rm dl}$ values among xh_ANF to be accurate. Considering that the $C_{\rm dl}$ from EIS was obtained under positive potential when the conductive NiOOH phase is formed, whereas $C_{\rm dl}$ from CV was obtained when xh_ANF remains nonconductive, ²⁴ we decided to use $C_{\rm dl}$ from EIS as a reliable indicator for the electrochemical active surface area of the electrocatalyst in this study. The R_{ct} value decreased with anodization time as the active surface area (or $C_{\rm dl}$) increased, corresponding to the $j_{\rm OER}$ trend obtained from CV. On the contrary, the $R_{\rm et}$ value increased with anodization time probably due to the growing thickness of the porous oxide layer which electrons must pass through to reach the active sites at the surface to take part in the reaction. Additionally, it was observed that the $C_{\rm dl}$ value and OER activity of 7h_ANF decreased compared to 5h_ANF, as shown in Figure S10b-d. The electrochemical data and surface morphology of 7h_ANF in Figures S4 and S10 indicate the collapse of the nanoporous structure after the prolonged 7 h anodization. Therefore, further study was focused on xh ANF samples within a 5 h

When the value of j_{OER} at 1.73 V_{RHE} was plotted with regard to C_{dl} obtained from EIS, the value of j_{OER} increased almost linearly with C_{dl} values (Figure 3c). This result suggests the lack of a significant limitation from electron and mass transport

even for the high surface area electrocatalysts like 5h ANF operating at a current density above 300 mA/cm². Figure 3d shows the correlation between C_{dl} , j_{OER} , specific OER current density ($j_{OER,specific}$ which is defined as j_{OER}/C_{dl}), and anodization time. Note that iR compensation during CV measurements for the porous electrode (xh ANF) under a nonworking potential (0.924 V_{RHE}) only includes "compensation for solution resistance of the electrolyte" and not the compensation of "Ret of the catalyst electrode", implying that j_{OER} reflects the influence of electron transport properties for xh ANF. 22,24 It was observed that the value of $j_{OER,specific}$ slightly diminished with anodization time as Ret increased with anodization time. However, this relatively insignificant decrease in $j_{OER,specific}$ with C_{dl} compared to the dramatic increase in j_{OER} with C_{dl} accounts for the linear increase in j_{OER} with $C_{\rm dl}$.

After OER testing via CV in the potential range of 1.1 V_{RHE} to 1.73 V_{RHE} in Fe-free 1 M KOH electrolyte, XPS analysis using a Mg source was carried out to characterize the composition of bare NF and xh_ANF samples. Figures S15 and S16 show that bare NF and xh ANF do not contain any F 1s or Fe 2p signal and have the same Ni 2p spectra that corresponds to $NiO_x(OH)_y$, which indicates that OER testing was conducted in a well-purified Fe-free electrolyte and that the F-doping was removed from the xh ANF samples during OER testing. Also, XRD spectra and SEM images in Figures S17 and S18 indicate that the porous $NiO_x(OH)_y$ layer has amorphous structure and the nanoporous structures of xh ANF are well-maintained during OER testing in Fe-free KOH electrolyte. Consequently, the results from electrochemical analyses and material characterizations suggest that the morphological engineering of NF via anodization was effective for Fe-free $NiO_x(OH)_y$ to grow a large surface area while maintaining good electron and mass transport properties even under high operating current densities (~320 mA/cm²), which can be attributed to its self-templating synthesis and hierarchical porous structure.

Electrochemical Analyses in Unpurified 1 M KOH **Electrolyte.** The electrochemical characteristics and OER activity of xh ANF samples were also investigated in unpurified (Fe-containing) 1 M KOH electrolyte. Before the OER activity was compared, precycling through CV was conducted in the potential range of 1.1 to 1.58 V_{RHE} until the CV curves reached a steady state. From the CV curves in Figure 4a, the redox peak for the Ni²⁺ to Ni³⁺ transition was positively shifted compared to the same peak in the Fe-free electrolyte (1.37 V_{RHE}) as a result of the incorporation of the Fe impurity into the xh ANF samples, whereas the redox peak for Ni⁴⁺ was no longer observed. ¹⁹ As in the Fe-free electrolyte, the OER activity of the xh ANF samples in unpurified electrolyte increased with anodization time, and the 5h ANF sample exhibited the highest OER activity of j_{OER} over 500 mA/cm² at low overpotentials below 350 mV, which is comparable to previously reported NiFe-based high performance OER electrocatalysts (Table S2). It is to be noted that the CV measurements for xh ANF shown in Figure 4a were carried out under static conditions without employing any gasdislodging processes (e.g., stirring by a magnetic bar), and there was no change in the OER activity regardless of forced convection, implying the facile bubble dissipation ability of xh_ANF even under nonconvective, high current density operation. This can be ascribed to the advantages of its hierarchical porous structure consisting of nanometer-sized

pores that increase the hydrophilicity of the surface, resulting in the decrease of the adhesive force of the gas bubble, as well as reduce the size of the bubble by a spatial confinement effect, and micrometer-sized pores that facilitate the removal of produced oxygen bubbles as described in the inset of Figure 4a. ^{28–31} The hydrophilicity of the surface was measured with the contact angle of KOH electrolyte droplet on the surface of bare NF and ANF samples (Figure S19). Whereas bare NF showed hydrophobic property with a contact angle of 85.9°, ANF samples immediately absorbed a KOH electrolyte droplet, implying its enhanced surface hydrophilicity.

To scrutinize the above OER activity trend, EIS analyses of xh_ANF samples in unpurified electrolyte were conducted at 1.58 V_{RHE} (Figure S20a). As shown in Figure 4b and Table S3, the same trend as in Fe-free electrolyte was observed; the R_{ct} value decreased with anodization time while the $C_{\rm dl}$ and $R_{\rm et}$ values increased with anodization time. The smaller R_{ct} and R_{et} values in the unpurified electrolyte compared with those in a Fe-free electrolyte can be ascribed to the higher intrinsic catalytic activity and electron transport properties of Fe-doped ANF compared to Fe-free ANF. 14,15,18,19 Figure S20b—e shows the obvious change in the EIS spectra to an asymmetric shape with anodization time, signifying that R_{et} negatively affected the OER activity noticeably despite its decreased value. Also, it was observed that $C_{\rm dl}$ values for xh_ANF samples obtained from both EIS and CV in unpurified electrolyte were higher than those in Fe-free electrolyte (Tables S1 and S3 and Figures S14 and S21). This might be related to an overestimation of the $C_{\rm dl}$ value owing to the complication from different specific capacitance values of $NiO_x(OH)_y$ and Fe-doped $NiO_x(OH)_y$.

When j_{OER} (at 1.58 V_{RHE}) is plotted against the C_{dl} value, as opposed to the linear trend in the Fe-free electrolyte, the value of j_{OER} in the unpurified electrolyte did not increase linearly with C_{dl} (Figure 4c). The deviation from linearity was consistent with the noticeable decrease in $j_{OER,specific}$ with increasing anodization time (Figure 4d). Considering that the same xh_ANF samples were employed for OER testing, it is worth investigating why the xh_ANF samples in Fe-free and unpurified electrolytes showed different results. This point will be discussed in detail later in the paper.

After OER testing in unpurified KOH electrolyte, XRD and SEM analyses were conducted to characterize the crystal structure and morphology of xh ANF samples. Figures S22 and S23 show that the Fe-doped $NiO_x(OH)_y$ layer has amorphous structure and the nanoporous structures of xh ANF are well-maintained during OER testing in unpurified KOH electrolyte. Furthermore, the stability of the 5h ANF sample with the highest OER activity was tested using chronopotentiometry (CP) analysis at a current density of 500 mA/cm². Figure 5 displays that the 5h ANF sample showed a negligible change in OER potential for 24 h, validating its excellent durability even under high current density operation. Additionally, to better reveal the morphological advantages of ANF in terms of electron transport, the control experiment was performed using a conventional catalyst film made of NiO nanoparticles (see Figures S24-26 and Table S4 for details).

Deviation from Linear Trend between j_{OER} and C_{dl} in Unpurified Electrolyte. In Figures 3c and 4c, the plots of j_{OER} values against those for C_{dl} in Fe-free and unpurified electrolytes showed different trends, even though the same xh_ANF samples were employed for OER testing in both electrolytes. Given that the C_{dl} values for xh_ANF samples in

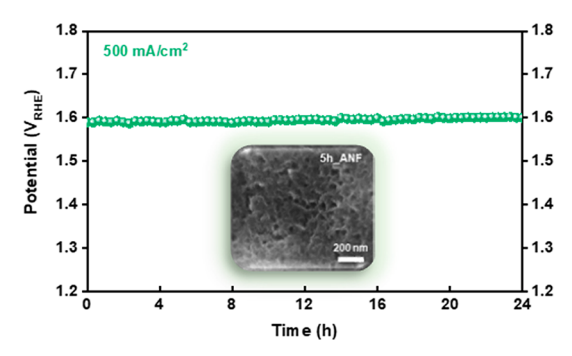


Figure 5. CP analysis of 5h_ANF at 500 mA/cm² for 24 h in unpurified 1 M KOH electrolyte (inset shows the SEM image of 5h ANF after CP test for 24 h).

unpurified electrolyte were higher than those in Fe-free electrolyte, there is a chance that the C_{dl} values in unpurified electrolyte were overestimated, possibly due to a complication from the distinct specific capacitance value of Fe-doped $NiO_x(OH)_v$ compared with that of Fe-free $NiO_x(OH)_v$. In this case, the overestimated value for C_{dl} can result in a lower value for $j_{\text{OER,specific}}$ in the unpurified electrolyte compared with their actual $j_{OER,specific}$ values, and it can thus contribute to the deviation from the linear trend of j_{OER} and C_{dl} . Nevertheless, when comparing the j_{OER} values in the two electrolytes, the j_{OER} values for xh ANF samples in the Fe-free electrolyte increased by \sim 16 times from 0 to 5 h, whereas the j_{OER} values in the unpurified electrolyte increased by only ~ 10 times. This confirms the decrease of the actual value for $j_{OER,specific}$ with anodization time in the unpurified electrolyte, which caused the deviation of j_{OER} from the linear relation with C_{dl} . To elucidate the origin of a noticeable $j_{OER,specific}$ value decrease with $C_{\rm dl}$ in the unpurified electrolyte, we considered three possible reasons: (1) different Fe incorporation, (2) mass transport limitation, and (3) electron transport limitation.

First, in terms of Fe incorporation, it is suspected that the ANF samples with higher C_{dl} values might have a lower Fe content, resulting in a decreased value for $j_{OER,specfic}$ as a function of C_{dl}. The surface Fe composition of the xh_ANF samples after OER testing in the unpurified electrolyte was analyzed using XPS with a Mg source by comparing the ratio of the integrated area of the Ni $2p_{3/2}$ spectra with that of the Fe 2p_{3/2} spectra (Figure S27 and Table S5). However, all of the xh ANF samples had almost the same Fe composition of around 11-12%. Nonetheless, there is still a possibility that nonuniform Fe incorporation occurs depending on the thickness of the ANF, such as a smaller Fe composition in the deeper side of the porous $NiO_x(OH)_y$ layer compared to the surface Fe composition. To confirm this possibility, the redox peak potential of xh ANF samples for the Ni²⁺ to Ni³⁺ transition in CV, which is indicative of the Fe concentration based on the degree of positive shift of the redox potential, was compared. However, as shown in Figure 4a, all of the xh_ANF samples showed the redox peak for the Ni^{2+} to Ni^{3+} transition at the same potential of 1.42 V_{RHE}, implying the same Fe composition for all of the xh_ANF samples. Also, this redox peak potential at 1.42 V_{RHE} coincides with the redox peak potential of previously reported Ni-based catalysts with a Fe composition of 10–15%. Furthermore, previous studies verified that Fe incorporation occurs not just at the surface but throughout the entire electrolyte-permeable $NiO_x(OH)_y$ layer within the thickness of 30-60 nm, as determined by

various depth profiling and composition characterization techniques. Given the open porous structure of the xh_ANF samples and their grain sizes on the scale of tens of nanometers (Figure S23), it is probable that Fe was well-incorporated through the electrolyte-permeable $\text{NiO}_x(\text{OH})_y$ layer, which is reflected in electrochemical C_{dl} measurement. Moreover, recent studies have identified that the surface Fe sites in $\text{Ni}_x\text{Fe}_{1-x}\text{OOH}$ are the catalytically active sites for OER and not the bulk Fe sites. Additionally, the surface Fe sites can be maintained during OER in the unpurified (Fe-containing) electrolyte. Considering that the surface that exists on the deeper side of the porous $\text{NiO}_x(\text{OH})_y$ layer can be well-exposed to the Fe impurity in the unpurified electrolyte and form surface Fe sites, it is unlikely that less Fe incorporation for thicker ANF samples would bring about a reduction in the value for $j_{\text{OER},\text{specific}}$.

To gain further insights into the depth-dependent distribution of Fe through the $\mathrm{NiO}_x(\mathrm{OH})_y$ layer, time-of-flight secondary ion mass spectrometry (TOF-SIMS) depth profiling combined with high-resolution imaging was performed on the Sh_ANF sample, which is the thickest among all of the xh_ANF samples, after OER testing in unpurified 1 M KOH. The detected signals of secondary ion fragments were normalized to their maximum and plotted against the sputter time, which qualitatively corresponds to the depth inside the electrode. Figure 6a shows the depth-dependent distribution of several ion species of interest (Ni^+ , $^{41}\mathrm{K}^+$, and Fe^+) inside the Sh_ANF sample consisting of a porous $\mathrm{NiO}_x(\mathrm{OH})_y$ layer supported by bulk Ni metal. It is to be noted that the Ni⁺ signal can result from both the porous $\mathrm{NiO}_x(\mathrm{OH})_y$ layer and

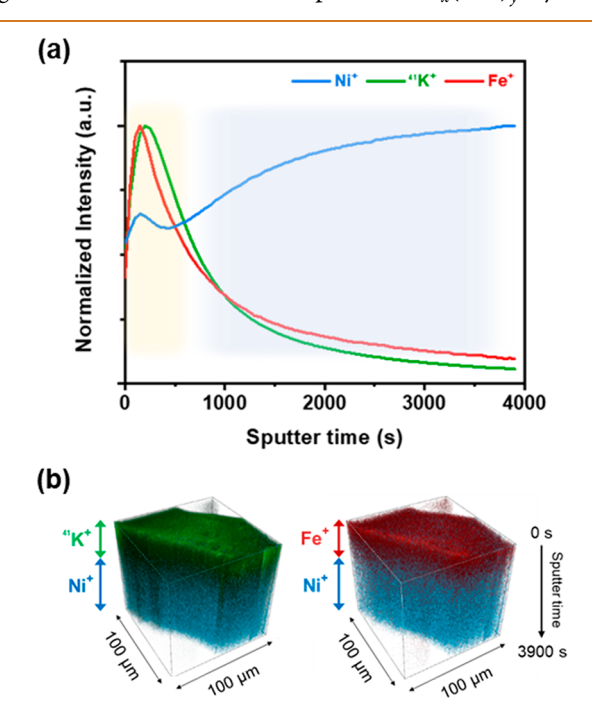


Figure 6. (a) TOF-SIMS depth profiles with high lateral resolution (normalized to maximum) of Ni⁺, 41 K⁺, and Fe⁺ for 5h_ANF after OER testing in unpurified 1 M KOH (yellow and blue shaded regions belong to porous NiO_x(OH)_y layer and underlying bulk Ni metal, respectively). (b) 3D view of the depth profiles showing the distribution of 41 K⁺ and Fe⁺ signals in porous NiO_x(OH)_y layer above the bulk Ni metal layer (Ni⁺ signal appears throughout the whole NiO_x(OH)_y/Ni layer).

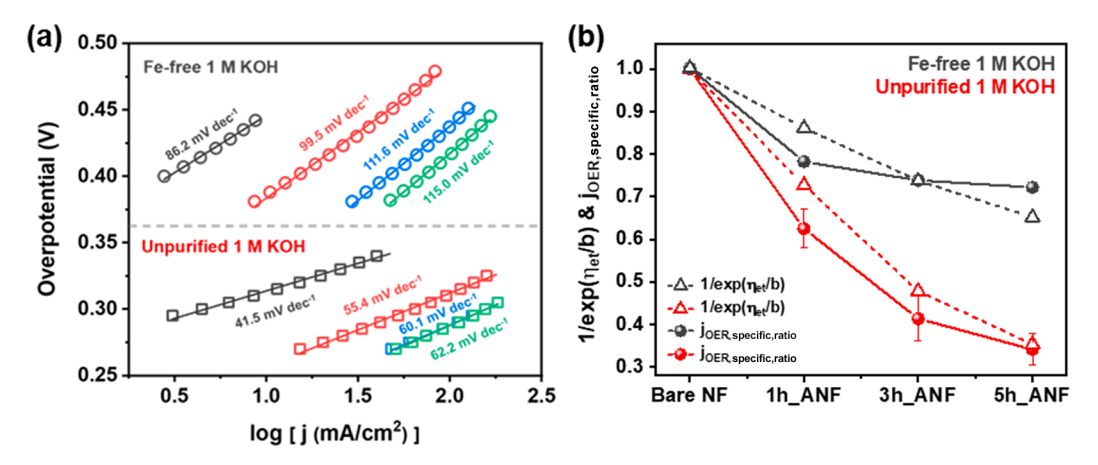


Figure 7. (a) Tafel plots of xh_ANF in Fe-free and unpurified 1 M KOH (black, red, blue, and green color correspond to bare NF, 1h_ANF, 3h_ANF, and 5h_ANF, respectively). (b) Comparison of $1/\exp(\eta_{\rm et}/b)$ and $j_{\rm OER, specific, ratio}$ (here, considering the overestimation of $C_{\rm dl}$ in unpurified electrolyte, $j_{\rm OER, specific, ratio}$ in unpurified electrolyte was calculated using $C_{\rm dl}$ in both Fe-free and unpurified electrolyte, and the average value with error bar was utilized).

bulk Ni metal. On the other hand, the ⁴¹K⁺ and Fe⁺ signals can only originate from the porous NiO_x(OH), layer, where K⁺ in KOH electrolyte is intercalated between the layered structure of NiO_x(OH)_y while the Fe impurity in the unpurified KOH electrolyte is incorporated into the lattice of $NiO_x(OH)_v$. ^{14,19} The Ni⁺ signal showed a small peak before ~450 s of sputter time, consistent with the maxima of the 41K+ and Fe+ depth profiles, thereby corresponding to the NiO_x(OH)_v layer. Considering the origin of each ion species and its depthdependent distribution described above, the yellow-shaded and blue-shaded regions depicted in Figure 6a correspond to the porous NiO_x(OH)_y layer and the supporting bulk Ni metal, respectively. Furthermore, the 41K+ and Fe+ ions exhibited almost identical depth-dependent profiles. Given that the presence of the 41K+ signal indicates the KOH electrolytepermeable region, the observed profiles of ⁴¹K⁺ and Fe⁺ imply that Fe was well-incorporated throughout the electrolytepermeable regions of the porous $NiO_x(OH)_y$ layer, where C_{dl} measurements were conducted, making the significant j_{OER,specific} value loss by nonuniform Fe incorporation unlikely. The 3D views of the TOF-SIMS depth profiles are delineated in Figure 6b, qualitatively confirming the virtually identical distribution of Fe⁺ and K⁺ in the porous NiO_x(OH)_y layer above the bulk Ni metal.

Second, in terms of mass transport, the supply of reactant (OH⁻) and removal of products (oxygen bubble) that should occur during the electrocatalytic reaction is determined by the operating current density. This implies the possibility that xh ANF samples in unpurified electrolyte could suffer from insufficient mass transport due to their operation at higher current densities compared to those in the Fe-free electrolyte, which demonstrates facile mass transport for its conditions. In this regard, to exclude any effect from a different mass transport limitation, j_{OER} at 1.55 V_{RHE} in unpurified electrolyte, which has a current density similar to that in the Fe-free electrolyte, was plotted against C_{dl}. As shown in Figure S28, the trend of the j_{OER} value versus C_{dl} in the unpurified electrolyte still exhibited a deviation from linearity, indicating that the mass transport limitation would not be the major cause for the noticeable reduction of the value for $j_{OER,specific}$ in the unpurified electrolyte.

Third, in terms of electron transport, considering that the $R_{\rm et}$ values in the unpurified electrolyte were lower than those in

the Fe-free electrolyte, the electron transport limitation might not seem to be the major cause for the significant decrease of $j_{\text{OER,specific}}$ value with C_{dl} in the unpurified electrolyte. To thoroughly examine the possibility of electron transport limitations, we investigated the impact of R_{et} on the overpotential loss caused by electron transport through the catalyst layer (η_{et}) and the resulting decrease in value of $j_{\text{OER,specific}}$ by η_{et} . The value of η_{et} can be expressed as shown in eq 1.24

$$\eta_{\rm et} = j_{\rm OER} \times R_{\rm et} \tag{1}$$

Also, we can express the "degree of decrease in $j_{OER,specific}$ value with anodization time" using the ratio of $j_{OER,specific}$ for xh_ANF samples to $j_{OER,specific}$ for bare NF ($j_{OER,specific,ratio}$) (eq 2)

$$j_{\text{OER, specific, ratio}} = \frac{j_{\text{OER, specific, xh_ANF}}}{j_{\text{OER, specific, bare NF}}}$$
(2)

Furthermore, we can also estimate the "degree of decrease in $j_{\text{OER,specific}}$ due to η_{et} " (estimated $j_{\text{OER,specific,ratio}}$) according to eqs 3–5.

$$j_{\text{OER,ideal at }\eta} = Aj_{\text{o}} \exp\left(\frac{\eta}{b}\right)$$
 (3)

$$j_{\text{OER,practical at }\eta} = Aj_{\text{o}} \exp\left(\frac{\eta - \eta_{\text{et}}}{b}\right) \tag{4}$$

estimated
$$j_{\text{OER,specific,ratio}} = \frac{j_{\text{OER,practical at }\eta}}{j_{\text{OER,ideal at }\eta}} = \frac{1}{\exp\left(\frac{\eta_{\text{et}}}{b}\right)}$$
 (5)

where η is the applied overpotential, $j_{\text{OER,ideal}}$ at η is the value of the ideal OER current density that is not affected by η_{et} $j_{\text{OER,practical}}$ at η is the OER current density that is affected by η_{et} j_{O} is the exchange current density, b is the Tafel slope, and A is the electrochemical active surface area of the catalyst electrode. Note that since A, which was estimated by C_{dl} in this study, should be in electrical contact with the current collector for the C_{dl} measurement, we regarded A as constant irrespective of η_{et}^{22} Equations 1 and 5 show that the value of j_{OER} and the Tafel slope can play a role in determining the actual contribution of R_{et} on the reduction of $j_{\text{OER,specific}}$; the larger the value of j_{OER} (the larger η_{et}) and the smaller the Tafel slope

are, the more impact $R_{\rm et}$ has on the reduction of the value of $I_{\rm OFR\ specific}$

In this regard, for the quantitative analysis of the impact of $R_{\rm et}$ on the decrease in $j_{\rm OER, specific}$, $\eta_{\rm et}$ and Tafel slope for the xh ANF samples in Fe-free and unpurified electrolytes were calculated (Figure 7a and Table S6). $\eta_{\rm et}$ values increased with anodization time as a result of increasing R_{et} and j_{OER} . Also, all xh_ANF samples in the Fe-free electrolyte showed $\eta_{\rm et}$ values higher than those in the unpurified electrolyte due to their larger Ret values. However, between the two electrolyte systems, the difference in $\eta_{\rm et}$ ratio was smaller than the difference in $R_{\rm et}$ ratio because of the higher $j_{\rm OER}$ in the unpurified electrolyte compared to that in the Fe-free electrolyte. In Figure 7a, the Tafel slope values for xh ANF samples in unpurified electrolyte were lower than those in Fefree electrolyte due to their higher intrinsic catalytic activity and electron transport properties. Also, the Tafel slope of the xh ANF samples in both Fe-free and unpurified electrolytes increased with anodization time. The increase in Tafel slope in the Fe-free electrolyte can be explained by increasing values for $R_{\rm et}$ with anodization time. On the other hand, the increase in the Tafel slope in the unpurified electrolyte can be affected by both an increase in Ret and a decrease in the intrinsic catalytic activity. However, considering the magnitude of increase in the Tafel slope with anodization time was smaller in unpurified electrolyte (20.7 mV dec⁻¹ between bare NF and the 5h_ANF sample) than in the Fe-free electrolyte (28.8 mV dec⁻¹ between bare NF and 5h_ANF), this result can be explained by the smaller $R_{\rm et}$ value in the unpurified electrolyte rather than changes in intrinsic catalytic activity.

Based on $\eta_{\rm et}$ and b, $\frac{1}{\exp(\frac{\eta_{\rm et}}{b})}$ was calculated and compared with

the $j_{\text{OER,specific,ratio}}$. Figure 7b presents that as anodization time increases, showing that the value of $\frac{1}{\exp\left(\frac{\eta_{\text{et}}}{b}\right)}$ for the unpurified

electrolyte decreased more steeply than that for the Fe-free electrolyte. This implies that the contribution of $R_{\rm et}$ to the decrease in the value of $j_{\rm OER,specific}$ is expected to be more significant for ANF in unpurified electrolyte compared to the ANF in Fe-free electrolyte, despite the lower $R_{\rm et}$ values. Also, the value of $j_{\rm OER,specific,ratio}$ followed nearly the same trend as $\frac{1}{\exp\left(\frac{\eta_{\rm et}}{b}\right)}$ and the difference in $\frac{1}{\exp\left(\frac{\eta_{\rm et}}{b}\right)}$ between Fe-free and

unpurified electrolytes closely matched with the difference in the value of $j_{\text{OER,specific,ratio}}$ between the two electrolytes, demonstrating the validity of using $\frac{1}{\exp\left(\frac{v_{\text{el}}}{b}\right)}$ as an indicator for

 $j_{\mathrm{OER,specific,ratio}}$. In short, all of these observations led to the conclusion that the electron transport limitation was the major cause for the noticeable decrease in $j_{\mathrm{OER,specific}}$ and the deviation from the linear trend in j_{OER} with the C_{dl} for Fe-doped ANF in unpurified electrolyte. This also suggests that R_{et} plays a more significant role in determining the OER activity for the Fe-doped ANF with higher intrinsic catalytic activity (lower Tafel slope) and higher operating current density compared to those of the Fe-free ANF.

CONCLUSION

In summary, we propose the morphological engineering of nickel foam *via* electrochemical anodization to create 3D hierarchical porous structures with large surface areas and variable thickness of the nanoporous layer. To uniformly grow

the nanoporous structure on the 3D NF substrate, the anodization condition was optimized to minimize the nonuniform localization of the e-field. Using two different compositions of electrocatalysts (Fe-free and Fe-doped ANF), we thoroughly investigated the influence of morphological engineering and the resulting transport properties on the OER activity as a function of surface area under high current densities. By elucidating the trends between j_{OER} and C_{dl} in the Fe-free and unpurified electrolytes, we demonstrated the essential role of electron transport for large surface area catalysts with good intrinsic catalytic activity and high operating current density (~500 mA/cm²). With regard to the design strategy for highly active electrocatalysts, the intrinsic catalytic activity has often been considered the most important among several parameters. However, the results from this study give us insight that improving the electron transport properties of a catalyst electrode should also be considered critical when designing high-performance electrocatalysts that are applicable for practical usage.

METHODS

Materials. Nickel foam with a thickness of 1.6 mm and a purity of 99.99% (MTI corporation) was used. Ethanol (99.5%, PHARMCO), ammonium fluoride (99.3%, Fisher), ethylene glycol (certified grade, Fisher), deionized (DI) water (18 M Ω), potassium hydroxide (90% flakes, Sigma-Aldrich), isopropyl alcohol (99.9%, Fisher), and Nafion (5 wt %, Sigma-Aldrich) were used without further purification.

Preparation of xh_ANF and NiO NP Film. The nickel foams were cleaned in ethanol and DI water (18 M Ω) for 10 min by ultrasonication. For electrochemical anodization, a two-electrode system consisting of nickel foam as the working electrode and Pt mesh as the counter electrode that are 2.5 cm apart from each other was used. Electrochemical anodization was carried out at 25 °C by applying 30 V for different amounts of time (e.g., 1, 3, 5, and 7 h). The optimized electrolyte for anodization contains 50 mM NH₄F and 4 vol % H₂O in ethylene glycol. After anodization, anodized samples were carefully rinsed with ethanol and DI water and dried in air. The NiO NP was synthesized according to a previous method using NiCl₂· $6H_2O$ as the starting material except that KOH was used instead of NaOH in this work. The NiO NP film for electrochemical analyses was fabricated on a glassy carbon electrode (0.19625 cm²) via a dropcasting method. An ink of NiO NP was prepared by ultrasonically dispersing 10 mg of NiO NP powder in a 1 mL solution of isopropyl alcohol (Fisher Scientific) with 1 wt % of Nafion perfluorinated ionexchange resin solution (5 wt %, Sigma-Aldrich). Subsequently, 30 μ L $(3 \mu L \times 10)$ of the as-prepared ink was cast on the glassy carbon electrode and dried under an ambient environment. The NiO NP film for material characterization was prepared on a titanium foil by drop casting the ink of NiO NP powder in isopropyl alcohol without Nafion solution.

Physicochemical Characterization. The crystal structure of prepared samples was characterized by X-ray diffraction (Ultima IV diffractometer, Rigaku) in a thin-film configuration equipped with Cu $K\alpha$ radiation ($\lambda = 1.540598$ Å) using 40 kV of generator voltage and 40 mA. Top-view and cross-sectional SEM images as well as EDX analysis results were obtained using a FEI Quanta 650 ESEM at an accelerating voltage of 30 kV and a vacuum of approximately 5×10^{-6} Torr. The cross section of the ANF electrode was prepared with an Ar-ion milling system (IM4000Plus, Hitachi). The TEM images and SAED pattern were obtained using JEOL 2010F high-resolution transmission electron microscope with a voltage of 200 kV and camera length of 40 cm. Surface chemical compositions of xh ANF samples before OER testing were checked by XPS (Axis Ultra DLD spectrometer, Kratos) using monochromatic Al K α radiation (1486.6 eV) with a spot size of 400 μ m. Also, after OER testing, to detect the low concentration Fe by avoiding overlapping of Ni LMM Auger features with the Fe 2p peaks for the Al source, XPS analysis (PHI 3057, Physical Electronics) using Mg K α radiation (1253.6 eV) was performed. All binding energies were adjusted to the adventitious carbon C 1s signal at 284.8 eV. A TOF-SIMS 5 by ION-TOF GmbH (2010) was used to observe the depth-dependent distribution of Ni, K, and Fe species. TOF-SIMS depth profiling combined with high-resolution imaging was performed in positive polarity detection mode using an ${\rm O_2}^+$ sputtering beam (1 keV ion energy, 170 nA measured sample current) to sputter a 300 × 300 $\mu{\rm m}^2$ area while a Bi⁺ analysis beam (30 keV ion energy, 0.4 pA measured sample current) was raster scanned over a 100 × 100 $\mu{\rm m}^2$ area with 256 × 256 pixel resolution centered within the ${\rm O}^{2+}$ sputtered area. The pressure of the analysis chamber was below 2 × 10⁻⁹ Torr during analysis. The contact angle of the KOH electrolyte droplet was measured with a FTA200 contact angle goniometer.

Electrochemical Measurements. Electrochemical analyses were carried out in both purified (Fe-free) and unpurified (containing Fe impurities) 1 M KOH electrolyte. An aqueous solution of 1 M KOH was prepared by dissolving the KOH solid salts in ultrapure DI water. For the preparation of Fe-free 1 M KOH electrolyte, 1 M KOH solution was purified according to the previous method using absorption of Fe by Ni(OH). A polypropylene container was washed with 0.5 M H₂SO₄ and DI water to remove any remaining impurities and then was employed as an electrochemical reactor to avoid any possible contamination (e.g., glass-etching in alkaline media). A Teflon-coated titanium (Ti) clip was used to connect the working electrode to a potentiostat. Electrochemical analyses were conducted using a CHI660D electrochemical workstation (CH Instrument, USA) with a three-electrode configuration. A Pt foil and Hg/HgO in 1 M KOH served as the counter electrode and reference electrode, respectively. The potential applied to the Hg/ HgO reference electrode ($E_{\rm Hg/HgO}$) was converted into the reversible hydrogen electrode (RHE) scale via the Nernst equation $[E_{RHE}]$ = $E_{\rm Hg/HgO}$ + 0.059 × pH + $E^{\circ}_{\rm Hg/HgO}$], where $E^{\circ}_{\rm Hg/HgO}$ in 1 M KOH at 25 °C is 0.098. The 85% of *iR* drop from uncompensated resistance $(R_{\rm u})$ was compensated during CV measurements. The OER activity was measured with CV at a scan rate of 10 mV/s in the potential range of 1.10-1.73 V for the Fe-free 1 M KOH electrolyte system and 1.10-1.58 V for the unpurified electrolyte system. Also, CV in the nonfaradaic potential range of 0.727–0.827 \dot{V}_{RHE} was carried out at five different scan rates (1, 2, 5, 10, and 25 mV) to estimate C_{dl} of nonconductive ANF from the scan rate dependence of double layer charging $[\Delta j/2 = (j_a - j_c)/2$. EIS was measured in the frequency range from 5×10^{-2} to 10^6 Hz with 10 mV of amplitude at 1.63 V for the Fe-free system and 1.58 V for the unpurified system. Chronopotentiometry was carried out for 24 h at 500 mA/cm² for the stability test.

ASSOCIATED CONTENT

Supporting Information

The Supporting Information is available free of charge at https://pubs.acs.org/doi/10.1021/acsnano.0c10788.

Experimental details, digital photographs of prepared xh_ANF samples, EDX point analysis for ANF synthesized by non-optimized anodization condition, TEM and SAED pattern, figures of XPS, XRD, and SEM for xh_ANF samples before and after OER testing in Fefree and unpurified KOH electrolytes, contact angle measurements of a KOH electrolyte droplet on bare NF and xh_ANF, figures and tables of CV and EIS data as well as the corresponding equivalent circuit models for EIS fitting (PDF)

AUTHOR INFORMATION

Corresponding Author

C. Buddie Mullins – McKetta Department of Chemical Engineering, Department of Chemistry, and H2@UT, The University of Texas at Austin, Austin, Texas 78712, United States; orcid.org/0000-0003-1030-4801; Email: mullins@che.utexas.edu

Authors

Yoon Jun Son — McKetta Department of Chemical Engineering, The University of Texas at Austin, Austin, Texas 78712, United States

Kenta Kawashima — Department of Chemistry, The University of Texas at Austin, Austin, Texas 78712, United States; orcid.org/0000-0001-7318-6115

Bryan R. Wygant – Department of Chemistry, The University of Texas at Austin, Austin, Texas 78712, United States

Chon Hei Lam – McKetta Department of Chemical Engineering, The University of Texas at Austin, Austin, Texas 78712, United States

James N. Burrow — McKetta Department of Chemical Engineering, The University of Texas at Austin, Austin, Texas 78712, United States

Hugo Celio – Texas Materials Institute, The University of Texas at Austin, Austin, Texas 78712, United States

Andrei Dolocan — Texas Materials Institute, The University of Texas at Austin, Austin, Texas 78712, United States;
ocid.org/0000-0001-5653-0439

John G. Ekerdt — McKetta Department of Chemical Engineering, The University of Texas at Austin, Austin, Texas 78712, United States; orcid.org/0000-0002-1788-5330

Complete contact information is available at: https://pubs.acs.org/10.1021/acsnano.0c10788

Notes

The authors declare no competing financial interest.

ACKNOWLEDGMENTS

The authors gratefully acknowledge the National Science Foundation *via* grants CHE-1664941 (C.B.M.) and CMMI-1728656 (J.G.E.) as well as the Welch Foundation for their generous support through Grant No. F-1436 (C.B.M). Y.J.S. acknowledges the Kwanjeong Educational Foundation Scholarship in South Korea.

REFERENCES

- (1) Dau, H.; Limberg, C.; Reier, T.; Risch, M.; Roggan, S.; Strasser, P. The Mechanism of Water Oxidation: From Electrolysis *via* Homogeneous to Biological Catalysis. *ChemCatChem* **2010**, 2, 724–761.
- (2) Laha, S.; Lee, Y.; Podjaski, F.; Weber, D.; Duppel, V.; Schoop, L. M.; Pielnhofer, F.; Scheurer, C.; Müller, K.; Starke, U.; Reuter, K.; Lotsch, B. V. Ruthenium Oxide Nanosheets for Enhanced Oxygen Evolution Catalysis in Acidic Medium. *Adv. Energy Mater.* **2019**, *9*, 1803795.
- (3) Seitz, L. C.; Dickens, C. F.; Nishio, K.; Hikita, Y.; Montoya, J.; Doyle, A.; Kirk, C.; Vojvodic, A.; Hwang, H. Y.; Norskov, J. K.; Jaramillo, T. F. A Highly Active and Stable IrO_x/SrIrO₃ Catalyst for the Oxygen Evolution Reaction. *Science* **2016**, *353*, 1011–1014.
- (4) Suen, N.-T.; Hung, S.-F.; Quan, Q.; Zhang, N.; Xu, Y.-J.; Chen, H. M. Electrocatalysis for the Oxygen Evolution Reaction: Recent Development and Future Perspectives. *Chem. Soc. Rev.* **2017**, *46*, 337–365.
- (5) Kim, J.-H.; Youn, D. H.; Kawashima, K.; Lin, J.; Lim, H.; Mullins, C. B. An Active Nanoporous Ni(Fe) OER Electrocatalyst *via* Selective Dissolution of Cd in Alkaline Media. *Appl. Catal., B* **2018**, 225, 1–7.
- (6) Subbaraman, R.; Tripkovic, D.; Chang, K.-C.; Strmcnik, D.; Paulikas, A. P.; Hirunsit, P.; Chan, M.; Greeley, J.; Stamenkovic, V.; Markovic, N. M. Trends in Activity for the Water Electrolyser

- Reactions on 3d M(Ni,Co,Fe,Mn) Hydr(oxy)Oxide Catalysts. *Nat. Mater.* **2012**, *11*, 550–557.
- (7) McCrory, C. C. L.; Jung, S.; Peters, J. C.; Jaramillo, T. F. Benchmarking Heterogeneous Electrocatalysts for the Oxygen Evolution Reaction. *J. Am. Chem. Soc.* **2013**, *135*, 16977–16987.
- (8) Jin, S. Are Metal Chalcogenides, Nitrides, and Phosphides Oxygen Evolution Catalysts or Bifunctional Catalysts? *ACS Energy Lett.* **2017**, *2*, 1937–1938.
- (9) Wygant, B. R.; Kawashima, K.; Mullins, C. B. Catalyst or Precatalyst? The Effect of Oxidation on Transition Metal Carbide, Pnictide, and Chalcogenide Oxygen Evolution Catalysts. *ACS Energy Lett.* **2018**, *3*, 2956–2966.
- (10) Dionigi, F.; Strasser, P. NiFe-Based (Oxy)Hydroxide Catalysts for Oxygen Evolution Reaction in Non-Acidic Electrolytes. *Adv. Energy Mater.* **2016**, *6*, 1600621.
- (11) Roy, C.; Sebok, B.; Scott, S. B.; Fiordaliso, E. M.; Sørensen, J. E.; Bodin, A.; Trimarco, D. B.; Damsgaard, C. D.; Vesborg, P. C. K.; Hansen, O.; Stephens, I. E. L.; Kibsgaard, J.; Chorkendorff, I. Impact of Nanoparticle Size and Lattice Oxygen on Water Oxidation on NiFeO x H y. Nat. Catal. 2018, 1, 820–829.
- (12) Kou, T.; Wang, S.; Hauser, J. L.; Chen, M.; Oliver, S. R. J.; Ye, Y.; Guo, J.; Li, Y. Ni Foam-Supported Fe-Doped β -Ni(OH)₂ Nanosheets Show Ultralow Overpotential for Oxygen Evolution Reaction. *ACS Energy Lett.* **2019**, *4*, 622–628.
- (13) Li, M.; Liu, T.; Yang, Y.; Qiu, W.; Liang, C.; Tong, Y.; Li, Y. Zipping Up NiFe(OH)_x-Encapsulated Hematite to Achieve an Ultralow Turn-On Potential for Water Oxidation. *ACS Energy Lett.* **2019**, *4*, 1983–1990.
- (14) Friebel, D.; Louie, M. W.; Bajdich, M.; Sanwald, K. E.; Cai, Y.; Wise, A. M.; Cheng, M.-J.; Sokaras, D.; Weng, T.-C.; Alonso-Mori, R.; Davis, R. C.; Bargar, J. R.; Nørskov, J. K.; Nilsson, A.; Bell, A. T. Identification of Highly Active Fe Sites in (Ni,Fe)OOH for Electrocatalytic Water Splitting. *J. Am. Chem. Soc.* **2015**, *137*, 1305–1313.
- (15) Ahn, H. S.; Bard, A. J. Surface Interrogation Scanning Electrochemical Microscopy of $Ni_{1-x}Fe_xOOH$ (0 < x < 0.27) Oxygen Evolving Catalyst: Kinetics of the "Fast" Iron Sites. *J. Am. Chem. Soc.* **2016**, 138, 313–318.
- (16) Chung, D. Y.; Lopes, P. P.; Farinazzo Bergamo Dias Martins, P.; He, H.; Kawaguchi, T.; Zapol, P.; You, H.; Tripkovic, D.; Strmcnik, D.; Zhu, Y.; Seifert, S.; Lee, S.; Stamenkovic, V. R.; Markovic, N. M. Dynamic Stability of Active Sites in Hydr(oxy)-Oxides for the Oxygen Evolution Reaction. *Nat. Energy* **2020**, *5*, 222–230.
- (17) Klaus, S.; Cai, Y.; Louie, M. W.; Trotochaud, L.; Bell, A. T. Effects of Fe Electrolyte Impurities on Ni(OH)₂/NiOOH Structure and Oxygen Evolution Activity. *J. Phys. Chem. C* **2015**, *119*, 7243–7254.
- (18) Corrigan, D. A. The Catalysis of the Oxygen Evolution Reaction by Iron Impurities in Thin Film Nickel Oxide Electrodes. *J. Electrochem. Soc.* **1987**, 134, 377.
- (19) Trotochaud, L.; Young, S. L.; Ranney, J. K.; Boettcher, S. W. Nickel–Iron Oxyhydroxide Oxygen-Evolution Electrocatalysts: The Role of Intentional and Incidental Iron Incorporation. *J. Am. Chem. Soc.* **2014**, *136*, *6744*–*6753*.
- (20) Seh, Z. W.; Kibsgaard, J.; Dickens, C. F.; Chorkendorff, I.; Nørskov, J. K.; Jaramillo, T. F. Combining Theory and Experiment in Electrocatalysis: Insights into Materials Design. *Science* **2017**, 355, No. eaad4998.
- (21) Morales-Guio, C. G.; Liardet, L.; Hu, X. Oxidatively Electrodeposited Thin-Film Transition Metal (Oxy)Hydroxides as Oxygen Evolution Catalysts. *J. Am. Chem. Soc.* **2016**, *138*, 8946–8957.
- (22) Chung, D. Y.; Park, S.; Lopes, P. P.; Stamenkovic, V. R.; Sung, Y.-E.; Markovic, N. M.; Strmcnik, D. Electrokinetic Analysis of Poorly Conductive Electrocatalytic Materials. *ACS Catal.* **2020**, *10*, 4990–4996.
- (23) Bediako, D. K.; Costentin, C.; Jones, E. C.; Nocera, D. G.; Savéant, J.-M. Proton-Electron Transport and Transfer in Electro-

- catalytic Films. Application to a Cobalt-Based O₂-Evolution Catalyst. *J. Am. Chem. Soc.* **2013**, *135*, 10492–10502.
- (24) Batchellor, A. S.; Boettcher, S. W. Pulse-Electrodeposited Ni–Fe (Oxy)Hydroxide Oxygen Evolution Electrocatalysts with High Geometric and Intrinsic Activities at Large Mass Loadings. *ACS Catal.* **2015**, *5*, 6680–6689.
- (25) Lu, X.; Zhao, C. Electrodeposition of Hierarchically Structured Three-Dimensional Nickel—Iron Electrodes for Efficient Oxygen Evolution at High Current Densities. *Nat. Commun.* **2015**, *6*, 6616.
- (26) Zhou, H.; Yu, F.; Zhu, Q.; Sun, J.; Qin, F.; Yu, L.; Bao, J.; Yu, Y.; Chen, S.; Ren, Z. Water Splitting by Electrolysis at High Current Densities under 1.6 V. Energy Environ. Sci. 2018, 11, 2858–2864.
- (27) Liu, G.; Wang, M.; Wu, Y.; Li, N.; Zhao, F.; Zhao, Q.; Li, J. 3D Porous Network Heterostructure NiCe@NiFe Electrocatalyst for Efficient Oxygen Evolution Reaction at Large Current Densities. *Appl. Catal., B* **2020**, *260*, 118199.
- (28) Wang, J.; Zheng, Y.; Nie, F.-Q.; Zhai, J.; Jiang, L. Air Bubble Bursting Effect of Lotus Leaf. *Langmuir* 2009, 25, 14129–14134.
- (29) Lu, Z.; Zhu, W.; Yu, X.; Zhang, H.; Li, Y.; Sun, X.; Wang, X.; Wang, H.; Wang, J.; Luo, J.; Lei, X.; Jiang, L. Ultrahigh Hydrogen Evolution Performance of Under-Water "Superaerophobic" MoS₂ Nanostructured Electrodes. *Adv. Mater.* **2014**, *26*, 2683–2687.
- (30) Faber, M. S.; Dziedzic, R.; Lukowski, M. A.; Kaiser, N. S.; Ding, Q.; Jin, S. High-Performance Electrocatalysis Using Metallic Cobalt Pyrite (CoS₂) Micro- and Nanostructures. *J. Am. Chem. Soc.* **2014**, *136*, 10053–10061.
- (31) Kim, S.; Ahn, C.; Cho, Y.; Hyun, G.; Jeon, S.; Park, J. H. Suppressing Buoyant Force: New Avenue for Long-Term Durability of Oxygen Evolution Catalysts. *Nano Energy* **2018**, *54*, 184–191.
- (32) Vrubel, H.; Moehl, T.; Grätzel, M.; Hu, X. Revealing and Accelerating Slow Electron Transport in Amorphous Molybdenum Sulphide Particles for Hydrogen Evolution Reaction. *Chem. Commun.* **2013**, *49*, 8985–8987.
- (33) Skeldon, P.; Thompson, G. E.; Garcia-Vergara, S. J.; Iglesias-Rubianes, L.; Blanco-Pinzon, C. E. A Tracer Study of Porous Anodic Alumina. *Electrochem. Solid-State Lett.* **2006**, *9*, B47.
- (34) Kang, J. S.; Choi, H.; Kim, J.; Park, H.; Kim, J.-Y.; Choi, J.-W.; Yu, S.-H.; Lee, K. J.; Kang, Y. S.; Park, S. H.; Cho, Y.-H.; Yum, J.-H.; Dunand, D. C.; Choe, H.; Sung, Y.-E. Multidimensional Anodized Titanium Foam Photoelectrode for Efficient Utilization of Photons in Mesoscopic Solar Cells. *Small* **2017**, *13*, 1701458.
- (35) Hebert, K. R.; Albu, S. P.; Paramasivam, I.; Schmuki, P. Morphological Instability Leading to Formation of Porous Anodic Oxide Films. *Nat. Mater.* **2012**, *11*, 162–166.
- (36) Lee, C.-Y.; Lee, K.; Schmuki, P. Anodic Formation of Self-Organized Cobalt Oxide Nanoporous Layers. *Angew. Chem., Int. Ed.* **2013**, *52*, 2077–2081.
- (37) Shahzad, K.; Tsuji, E.; Aoki, Y.; Nagata, S.; Habazaki, H. Formation and Field-Assisted Dissolution of Anodic Films on Iron in Fluoride-Containing Organic Electrolyte. *Electrochim. Acta* **2015**, *151*, 363–369.
- (38) Yang, Y.; Fei, H.; Ruan, G.; Xiang, C.; Tour, J. M. Efficient Electrocatalytic Oxygen Evolution on Amorphous Nickel-Cobalt Binary Oxide Nanoporous Layers. *ACS Nano* **2014**, *8*, 9518–9523.
- (39) Kang, J. S.; Kim, J.; Kim, J. S.; Nam, K.; Jo, H.; Son, Y. J.; Kang, J.; Jeong, J.; Choe, H.; Kwon, T.-H.; Sung, Y.-E. Electrochemically Synthesized Mesoscopic Nickel Oxide Films as Photocathodes for Dye-Sensitized Solar Cells. ACS Appl. Energy Mater. 2018, 1, 4178–4185.
- (40) Grosvenor, A. P.; Biesinger, M. C.; Smart, R. St. C.; McIntyre, N. S. New Interpretations of XPS Spectra of Nickel Metal and Oxides. *Surf. Sci.* **2006**, *600*, 1771–1779.
- (41) Mansour, A. N. Characterization of B-Ni(OH)₂ by XPS. Surf. Sci. Spectra 1994, 3, 239–246.
- (42) Mansour, A. N. Characterization of NiO by XPS. Surf. Sci. Spectra 1994, 3, 231–238.
- (43) Xiong, D.; Li, W.; Liu, L. Vertically Aligned Porous Nickel(II) Hydroxide Nanosheets Supported on Carbon Paper with Long-Term Oxygen Evolution Performance. *Chem. Asian J.* **2017**, *12*, 543–551.

- (44) Koshtyal, Y.; Nazarov, D.; Ezhov, I.; Mitrofanov, I.; Kim, A.; Rymyantsev, A.; Lyutakov, O.; Popovich, A.; Maximov, M. Atomic Layer Deposition of NiO to Produce Active Material for Thin-Film Lithium-Ion Batteries. *Coatings* **2019**, *9*, 301.
- (45) Li, J.; Luo, F.; Zhao, Q.; Li, Z.; Yuan, H.; Xiao, D. Coprecipitation Fabrication and Electrochemical Performances of Coral-Like Mesoporous NiO Nanobars. *J. Mater. Chem. A* **2014**, *2*, 4690–4697.
- (46) Hussain, N.; Yang, W.; Dou, J.; Chen, Y.; Qian, Y.; Xu, L. Ultrathin Mesoporous F-Doped α -Ni(OH)2 Nanosheets as an Efficient Electrode Material for Water Splitting and Supercapacitors. *J. Mater. Chem. A* **2019**, *7*, 9656–9664.
- (47) Yang, Y.; Ruan, G.; Xiang, C.; Wang, G.; Tour, J. M. Flexible Three-Dimensional Nanoporous Metal-Based Energy Devices. *J. Am. Chem. Soc.* **2014**, *136*, 6187–6190.
- (48) Chen, L.; Chang, J.; Zhang, Y.; Gao, Z.; Wu, D.; Xu, F.; Guo, Y.; Jiang, K. Fluorine Anion-Enriched Nickel Hydroxyl Oxide as an Efficient Oxygen Evolution Reaction Electrocatalyst. *Chem. Commun.* **2019**, *55*, 3406–3409.
- (49) Jin, M.; Zhang, G.; Yu, F.; Li, W.; Lu, W.; Huang, H. Sponge-Like Ni(OH)₂ NiF₂ Composite Film with Excellent Electrochemical Performance. *Phys. Chem. Chem. Phys.* **2013**, *15*, 1601–1605.
- (50) Yang, Y.; Li, L.; Ruan, G.; Fei, H.; Xiang, C.; Fan, X.; Tour, J. M. Hydrothermally Formed Three-Dimensional Nanoporous Ni-(OH), Thin-Film Supercapacitors. *ACS Nano* **2014**, *8*, 9622–9628.
- (51) Song, L.; Zhao, M.; Li, X.; Zhang, Z.; Qu, L. Solution-Processed MoS₂ Nanotubes/Reduced Graphene Oxide Nanocomposite as an Active Electrocatalyst toward the Hydrogen Evolution Reaction. RSC Adv. 2016, 6, 70740–70746.
- (52) Terezo, A. J.; Bisquert, J.; Pereira, E. C.; Garcia-Belmonte, G. Separation of Transport, Charge Storage and Reaction Processes of Porous Electrocatalytic IrO₂ and IrO₂/Nb₂O₅ Electrodes. *J. Electroanal. Chem.* **2001**, 508, 59–69.
- (53) Bisquert, J. Theory of the Impedance of Electron Diffusion and Recombination in a Thin Layer. J. Phys. Chem. B 2002, 106, 325–333.
- (54) Bisquert, J.; Garcia-Belmonte, G.; Fabregat-Santiago, F.; Ferriols, N. S.; Bogdanoff, P.; Pereira, E. C. Doubling Exponent Models for the Analysis of Porous Film Electrodes by Impedance. Relaxation of TiO₂ Nanoporous in Aqueous Solution. *J. Phys. Chem. B* **2000**, *104*, 2287–2298.
- (55) Fabregat-Santiago, F.; Bisquert, J.; Garcia-Belmonte, G.; Boschloo, G.; Hagfeldt, A. Influence of Electrolyte in Transport and Recombination in Dye-Sensitized Solar Cells Studied by Impedance Spectroscopy. Sol. Energy Mater. Sol. Cells 2005, 87, 117–131.
- (56) Smith, A. M.; Trotochaud, L.; Burke, M. S.; Boettcher, S. W. Contributions to Activity Enhancement *via* Fe Incorporation in Ni-(Oxy)Hydroxide/Borate Catalysts for Near-Neutral PH Oxygen Evolution. *Chem. Commun.* **2015**, *51*, 5261–5263.
- (57) Stevens, M. B.; Trang, C. D. M.; Enman, L. J.; Deng, J.; Boettcher, S. W. Reactive Fe-Sites in Ni/Fe(oxy)Hydroxide Are Responsible for Exceptional Oxygen Electrocatalysis Activity. *J. Am. Chem. Soc.* **2017**, *139*, 11361–11364.
- (58) Farhat, R.; Dhainy, J.; Halaoui, L. I. OER Catalysis at Activated and Codeposited NiFe-Oxo/Hydroxide Thin Films Is Due to Postdeposition Surface-Fe and Is Not Sustainable without Fe in Solution. *ACS Catal.* **2020**, *10*, 20–35.
- (59) Rahdar, A.; Aliahmad, M.; Azizi, Y. NiO Nanoparticles: Synthesis and Characterization. *J. Nanostructures* **2015**, *5*, 145–151.